



Microstructural Degradation and Creep Fracture Behavior of Conventionally and Thermomechanically Treated 9% Chromium Heat Resistant Steel

Javier Vivas¹ · Carlos Capdevila¹ · Eberhard Altstadt² · Mario Houska² · Ilchat Sabirov³ · David San-Martín¹

Received: 18 June 2018 / Accepted: 12 September 2018 / Published online: 26 September 2018
© The Korean Institute of Metals and Materials 2018

Abstract

The microstructural degradation and the creep fracture behavior of conventionally and thermomechanically treated Grade 91 steel were investigated after performing small punch creep tests. A remarkable reduction in creep ductility was observed for the samples thermomechanically treated in comparison to those conventionally treated under the tested conditions of load (200 N) and temperature (700 °C). A change in the fracture mechanism from a ductile transgranular fracture to a brittle intergranular fracture was observed when changing from the conventionally treated to the thermomechanically treated processing condition, leading to this drop in creep ductility. The change in the fracture mechanism was associated to the localized concentration of creep deformation, close to coarse $M_{23}C_6$ carbides, at the vicinity of prior austenite grain boundaries (PAGB) in the thermomechanically treated samples. The preferential recovery experienced at the vicinity of PAGB produced the loss of the lath structure and the coarsening of the $M_{23}C_6$ precipitates. The electron microscopy images provided suggest that the creep cavities nucleate in these weak recovered areas, associated to the presence of coarse $M_{23}C_6$. After the coalescence of the cavities the propagation of the cracks was facilitated by the large prior austenite grain size produced during the austenitization which favors the propagation of the cracks along grain boundaries triggering the intergranular brittle fracture. This fracture mechanism limits the potential use of the proposed thermomechanical processing routes.

Keywords Creep resistant steels · Thermomechanical treatment · Creep fracture behavior · Microstructural degradation · Small punch creep tests · Ausforming

1 Introduction

The conventional power plants present disadvantages of low efficiency and high CO₂ emissions. These important drawbacks, together with the increasing demand for energy, have enhanced the interest to rise the service temperature and pressure of the power plants. High Cr ferritic/martensitic steels are considered as a key material for this application

because of its excellent corrosion and oxidation resistance [1–4]. However, the main limitation for these materials to be used at higher operation temperatures is due to their low creep strength [5–7].

The initial microstructure of the conventionally treated G91 steel consists in a tempered martensitic microstructure with two kinds of precipitates. One of these kinds of precipitates is the $M_{23}C_6$ carbides, rich in Cr and Mo, which is located at prior austenite grain boundaries and lath boundaries. The other type is the MX carbonitrides, rich in V and Nb, which is found homogeneously distributed within the laths. Besides, this microstructure is characterized by a high density of dislocations induced by the martensitic transformation [8].

Previous works have demonstrated the potential of the thermomechanical treatments to improve the creep resistance of these steels through the dispersion of a high number density of stable MX nanoprecipitates [9–11]. Tamura et al. [12] demonstrated the higher effectiveness of these

✉ Javier Vivas
jvm@cenim.csic.es

¹ Materialia Research Group, Physical Metallurgy Department, Centro Nacional de Investigaciones Metalúrgicas (CENIM-CSIC), 28040 Madrid, Spain

² Structural materials and concerning, Helmholtz-Zentrum Dresden - Rossendorf (HZDR), 01328 Dresden, Germany

³ IMDEA Materials Institute, 28906 Madrid, Spain

Table 1 Chemical composition of the commercial G91 ferritic-martensitic steel

Elements	C	Si	Mn	Cr	Mo	V	Nb	Fe
wt%	0.09	0.32	0.60	8.76	0.86	0.18	0.07	Balance

Table 2 Heat treatments of G91-AR

Heat	Heat treatment
G91-AR	Normalization 1040/30 min tempering 730/60 min

precipitates compared to the $M_{23}C_6$ carbides and lath microstructures during creep. In our previous work [13] it was shown by means of Small Punch Creep Tests (SPCT) that thermo-mechanical treatments (TMT) lead to higher creep strength compared to that obtained after applying conventional heat treatments. At the same time a reduction of creep ductility and a susceptibility to brittle fracture was observed for the thermomechanically treated steels. However, the reason for this brittle behavior was not identified. For Ferritic/martensitic steels the aim of the processing route is to obtain a component with a tempered martensite microstructure with high creep strength and ductility. The level of ductility in plain bar, uniaxial tests is a design parameter for boiler steels and it is assumed that over 15% elongation to fracture will be available. The risk of fast burst fracture for the components has to be avoided [14, 15]. The fracture resistance is related to the microstructural features that promote the nucleation and growth of cavities. The factors that influence the nucleation and growth are the distribution of precipitates in the martensitic matrix (location), their size and shape. The inclusions and the presence of trace elements also play an important role on the formation and growth of creep cavities. This paper is focused on identifying the key microstructural factors that have produced the brittleness after the thermomechanical processing. Therefore, this work studies the microstructural changes that occur during the creep process. For this reason, after the SPCT, different samples thermomechanically and conventionally treated have been investigated systematically by Scanning electron microscopy (SEM) and electron backscatter diffraction (EBSD) to clarify the microstructural changes undergone by the matrix and the precipitates during creep that finally produce the characteristic creep fracture behavior.

2 Experimental Procedures

The chemical composition and conventional heat treatment of the commercial G91 FM steel used in this work is shown in Tables 1 and 2, respectively. The material was supplied by CIEMAT in the form of a plate with a thickness of 40 mm.

Table 3 Description of the code used for the thermomechanically treated samples

Samples	Ausforming temperature (°C)	Ausforming deformation (%)
G91-TMT 900_20	900	20
G91-TMT 900_40	900	40
G91-TMT 600_20	600	20

Table 4 Small punch creep tests parameters

Punch diameter $d=2r$ (mm)	Receiving hole diameter D (mm)	Lower die hole chamfer
2.5	4.0	0.2 mm \times 45°

The thermomechanical treatments simulations were carried out on 10 mm in length and 8 mm in diameter cylindrical samples by compression using a thermomechanical simulator. The thermomechanical treatments involve heating the samples at 1225 °C during 5 min. Then, the samples are cooled down to the ausforming temperature. The deformation applied was 20% at the ausforming temperature of 600 °C and 20% and 40% at the ausforming temperature of 900 °C. A strain rate of 0.1 s^{-1} is employed to introduce the deformation. Finally, the samples are tempered during 45 min at 740 °C. The heating rates are 5 °C/s and the cooling rates 50 °C/s. The code used in this work for the thermomechanically treated samples is described in Table 3.

The samples were prepared by standard metallographic techniques, polishing down to 1 μm with diamond paste for microstructural examination by light optical microscopy (LOM) and scanning electron microscopy (SEM). The microstructure was revealed using the Vilella's reagent which contains 5 ml hydrochloric acid, 1 g of picric acid and 100 ml of ethyl alcohol. This chemical etching discloses carbides, ferrite and delta-ferrite phases.

Due to the limited amount of material available after the thermomechanical treatments carried out in the thermomechanical simulator, the creep properties were investigated by means of Small Punch Creep tests (SPCT). Description of this technique is found elsewhere [16–21].

Small Punch creep tests (SPCT) were performed at 700 °C with the parameters described in Table 4. SPCT disc samples were initially cut transversally from the cylindrical samples (perpendicular to the height of the cylinders) with a thickness of 600 μm and a diameter of 8 mm. Then, the discs

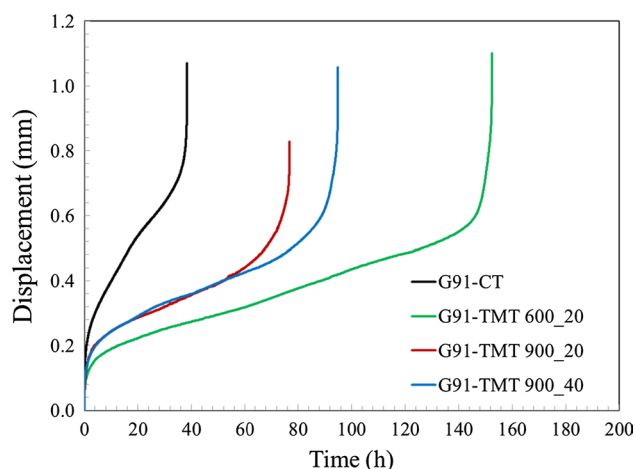


Fig. 1 SPCT curves for all samples tested at 700 °C with a load of 200 N

Table 5 Small punch creep results of the samples investigated

Samples	Minimum disk deflection rate ($\mu\text{m/h}$)	Time to rupture (h)
G91-AR	9.5	38.4
G91-TMT 900_20	3.2	76.8
G91-TMT 900_40	2.9	94.9
G91-TMT 600_20	2.0	152.5

were ground using a 1200 grit SiC paper down to a thickness of 500 μm . For detailed information on the SPCTs the reader is referred to [13].

EBSD (Electron Backscatter Diffraction) measurements were performed with a JEOL JSM 6500 FEG-SEM operating at 20 kV equipped with a fully automatic EBSD (Oxford Instruments HKL). Residual damage in the samples intended for the EBSD measurements, after diamond polishing, was removed through an additional polishing stage carried out with a colloidal silica solution (particle size ~ 40 nm). EBSD mapping has been carried out using step sizes of 0.4 μm . The HKL Channel 5 software has been employed for data processing.

3 Results and Discussion

Small Punch Creep displacement versus time curves, obtained at 700 °C using a load of 200 N, for the different samples under investigation are presented in Fig. 1. As can be seen in Table 5, from the results extracted in the Fig. 1, great difference in minimum disk deflection rate and time to rupture are observed for the different samples. As it was

reported by the authors in previous works [13, 22] these differences are explained based on the different number density of MX nanoprecipitates present in the microstructure. The higher number density of MX nanoprecipitates obtained by the deformation applied in austenite (ausforming) prior to tempering in the thermomechanical treatment allows reducing the minimum disk deflection rate and extends the time to rupture compared to the steel conventionally treated. The higher is the dislocation density obtained in ausformed fresh martensite the larger the number density of MX carbonitrides after tempering is, and in consequence, better creep strength is obtained.

Figure 2 provides several scanning electron micrographs of the fractured specimens after the SPCT for the different samples tested. Radial cracks can be observed in all the thermomechanically treated samples (Fig. 3a–c) indicating a brittle fracture and a change in rupture ductility in comparison to the conventional treated sample in which no radial cracks have been observed (Fig. 3d). Besides, a higher reduction in thickness is evident in the conventionally treated sample in comparison to the thermomechanically treated ones, suggesting a ductile fracture behavior. It is important to mention that no important differences in ductility have been noted among the thermomechanically treated samples. This information cannot be extracted from the creep curves in Fig. 1 by contrast with the conventional creep curves in tensile mode where smaller total elongation is associated with the reduction of creep ductility. This is because the small Punch Creep curves terminate when the ball is completely pushed through the disc, i.e. when the crack is opened to circular shape with a diameter of the ball. This stage is not identical with the onset of the macroscopic cracking (which occurs much earlier).

Figure 3 depicts scanning electron microscopy images of the different fracture surfaces with greater detail. For the conventional heat treated sample a characteristic dimple pattern of ductile fractures has been observed. This result correlates well the high reduction in the sample thickness shown previously (Fig. 2d). For the thermomechanically treated samples the dimple pattern has not been visualized and some cleavage facets are observed, which suggests that a brittle fracture has occurred. These brittle fracture surfaces match with the low reduction in thickness and the radial cracks shown in Fig. 2a–c).

To clarify the failure mechanisms, the fractured samples were cut and prepared adequately. As it can be seen, in the light optical images provided in Fig. 4, the conventionally treated sample exhibits transgranular cavities (Fig. 4a). By contrast, the thermomechanically treated samples ausformed at 600 °C and 900 °C with a deformation of 20%, Fig. 4b, c respectively, show the cavities growing mainly along and/or from the prior austenite grain boundaries (PAGB). This fact suggests that the degradation of the

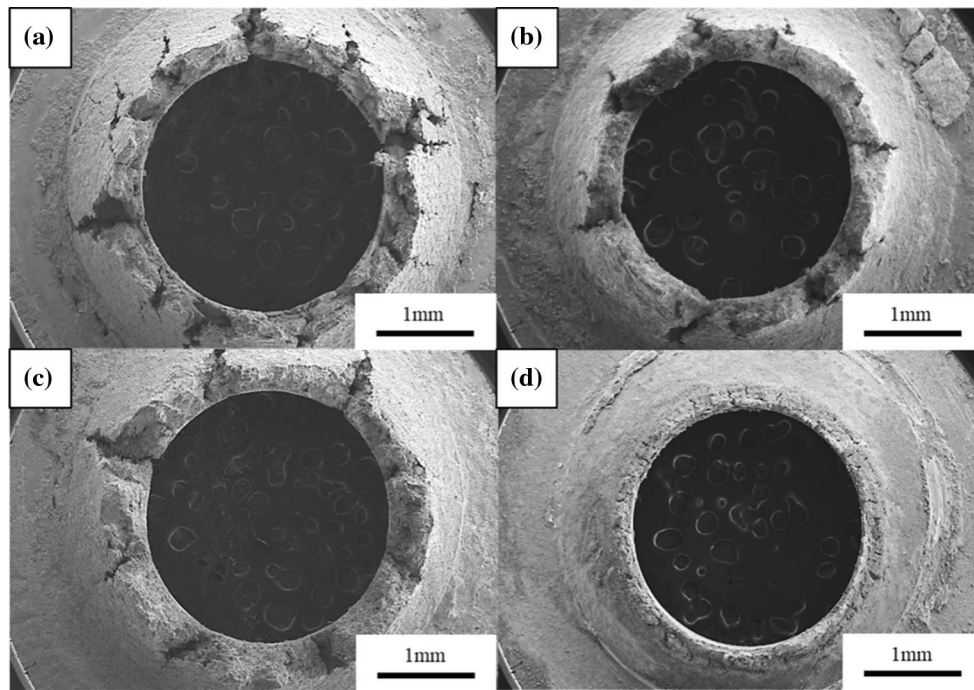


Fig. 2 Scanning electron microscopy images of the SPCT fracture surfaces for all samples tested at 700 °C with a load of 200 N **a** G91-TMT 900_20; **b** G91-TMT 600_20; **c** G91-TMT 900_40 and **d** G91-AR

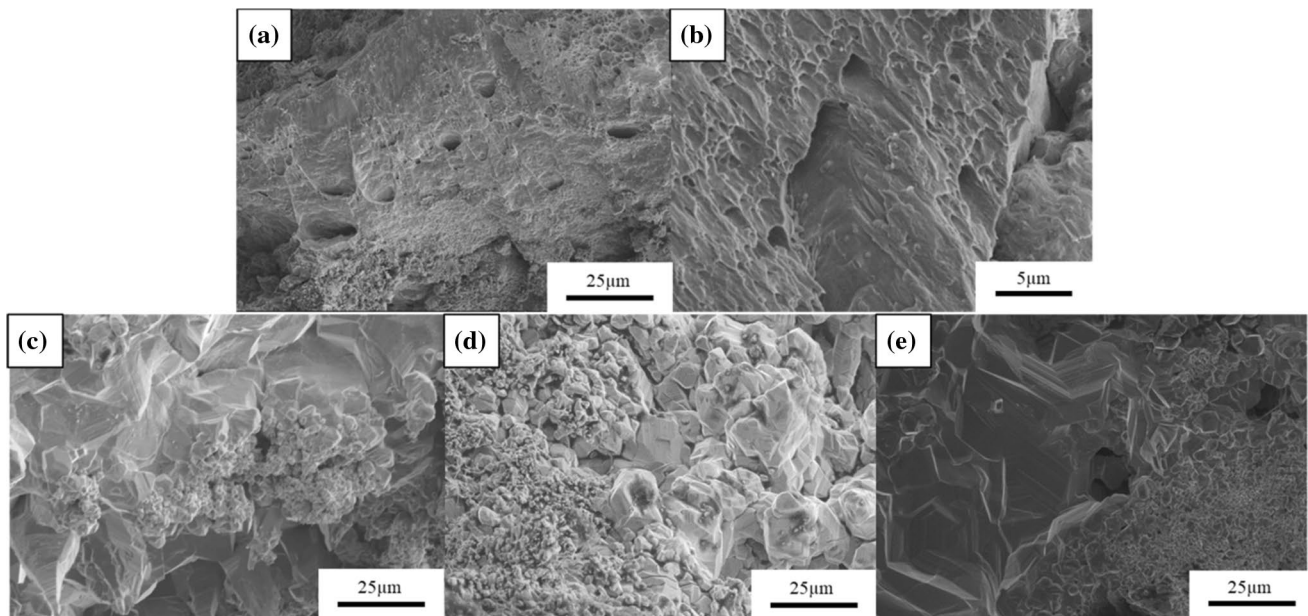


Fig. 3 Detailed scanning electron microscopy images of the SCPT fracture surfaces for all samples tested at 700 °C with a load of 200 N **a** G91-AR; **b** higher magnification of G91-AR; **c** G91-TMT 900_20; **d** G91-TMT 600_20 and **e** G91-TMT 900_40

microstructure occurs heterogeneously and starts at the vicinity of the PAGB for the thermomechanically treated samples. In contrast to this, the presence of transgranular cavities in the conventionally treated steel suggests that

during the SPCT the degradation of the microstructure happens homogeneously at random locations in the matrix.

Figure 5a, b show the SEM images for the thermo-mechanically treated samples ausformed at 600 °C with

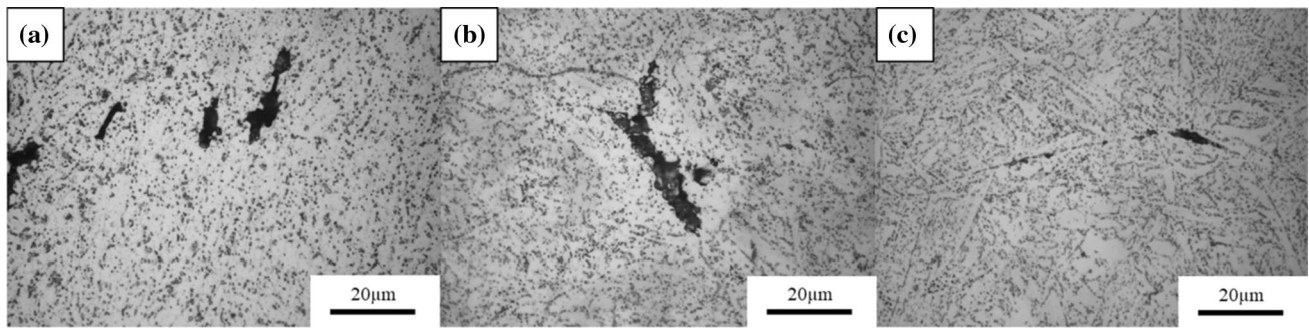


Fig. 4 Light optical images of the cavities location for **a** G91-AR; **b** G91-TMT 600_20 and **c** G91-TMT 900_20

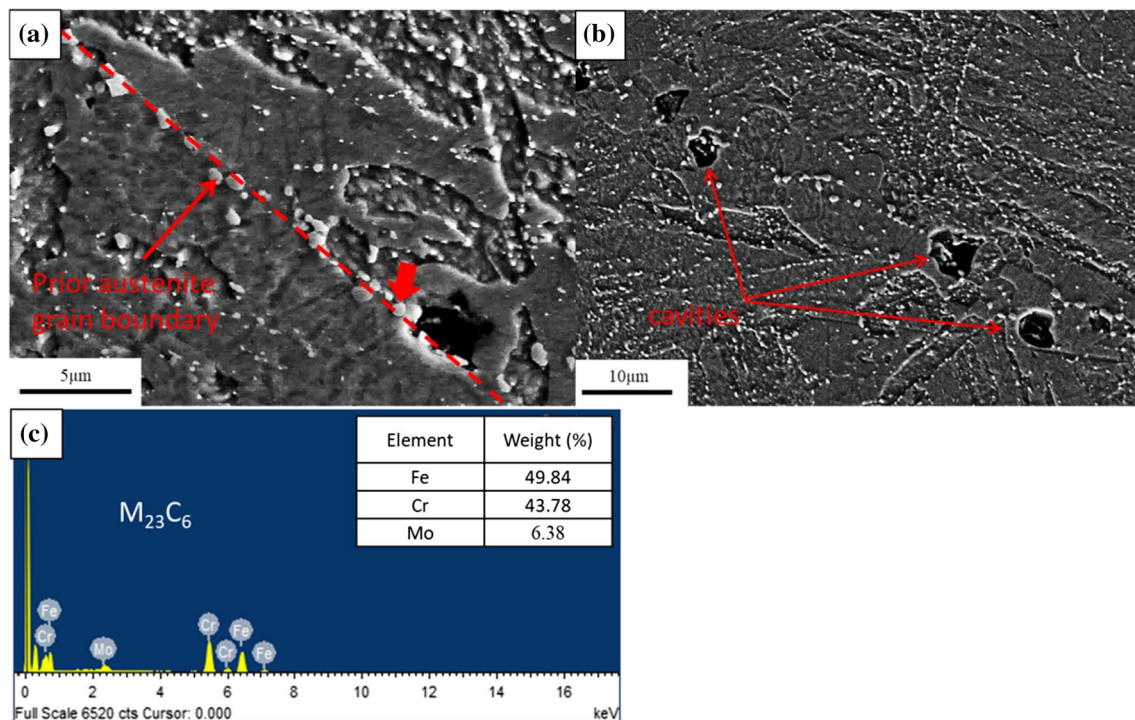


Fig. 5 Scanning electron microscopy images: **a** $M_{23}C_6$ precipitates located at a prior austenite grain boundary in sample G91-TMT 600_20. The prior austenite grain boundary in this image has been highlighted with a dash line as a guide to the eye; **b** cavities associ-

ated with coarse $M_{23}C_6$ precipitates have nucleated at a prior austenite grain boundary in sample G91-TMT 900_40. Cavities have been pinpointed with arrows; and **c** EDS analysis of the particle marked with a red arrow in image **a**, close to a cavity

a deformation of 20% and ausformed at 900 °C with a deformation of 40%. As it can be seen in these images, the cavities seem to be attached to coarse particles which are located at the vicinity of PAGBs. According to the EDS analysis carried out and displayed in Fig. 5c these particles are $M_{23}C_6$ carbides with $M = (Fe, Cr, Mo)$. The greater size of the $M_{23}C_6$ carbides at the vicinity of PAGB contributes to the inhomogeneous and localized deformation experienced by the thermomechanically treated samples at these locations during creep. As T. De Cock et al. [23] demonstrated in their work, coarse carbides are surrounded by a

deformation zone with a higher dislocation density than finer precipitates; this promotes the nucleation of strain-free grains, i.e., the formation of a recovered and equiaxed ferritic matrix. The high number density of MX nanoprecipitates achieved after the thermomechanical treatment produces high resistance to dislocation motion inside the grains and also could contribute to promote localized deformation in the vicinity of PAGBs. This mechanism, where the deformation accumulation is dominated by the localized deformation near grain boundaries, was reported in ODS steels where a high number density of obstacles

to dislocation motion within the grains is obtained by nano-oxides dispersion [24]. The local creep concentration close to PAGB would be promoting the nucleation of cavities that lead to the intergranular fracture with the brittle behavior shown previously in Fig. 2a–c.

Regarding the conventionally treated sample a homogeneous distribution of $M_{23}C_6$ carbides are observed in the whole sample as it is shown in Fig. 6. Hence, taking into account this observation and the uniform distribution of transgranular cavities, it may be deduced that a homogeneous distribution of creep deformation is obtained during the SPCT.

In Fig. 7a it is shown that around cavities small grains with a size of some microns have appeared during creep tests substituting the typical lath microstructure of these martensitic steels prior to creep. These small grains present an equiaxed shape and are pinned by fine $M_{23}C_6$ carbides. Also, as it can be seen in Fig. 7b, these small grains are observed in the conventionally heat treated sample. To better understand the formation of these small grains and to find out the microstructural degradation process during creep,

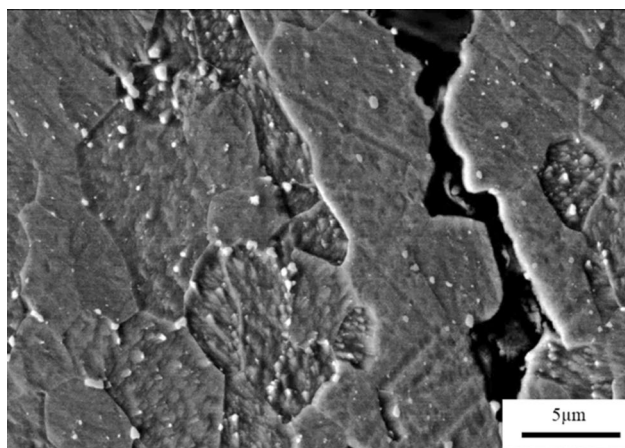


Fig. 6 Scanning electron microscopy image showing the presence of $M_{23}C_6$ carbides after SPCT for the sample G91-AR

different EBSD maps were performed in the samples under investigation.

Figure 8 shows different Inverse Pole Figure (IPF) maps for all the samples under study prior to SPCT. The block boundaries can be clearly distinguished but the lath boundaries are not correctly indexed due to the step size used for the EBSD mapping. The microstructures of the samples exhibit the characteristic lath-like shape morphology for martensite except for the steels ausformed at the lowest ausforming temperature in which this lath-like morphology is blurred as a result of the high deformation accumulated in the austenite during ausforming [25]. The ausformed microstructures (Fig. 8b–d) show a homogeneous microstructure similar to that observed after the conventional treatment (as-received sample Fig. 8a), where significant texture or microstructural directionality are not observed. This is explained through the fact that the deformation is applied to the austenite, upon its transformation to martensite during quenching any trace of texture produced in the austenite is lost.

Figure 9 shows the microstructures after SPCT for all samples investigated. In Fig. 9a a fine grain equiaxed ferritic matrix is observed for the material after conventional treatment. By contrast in Figs. 9b–d it can be seen that the original lath-like morphology has partially disappeared and, it has evolved towards a fine-grained equiaxed ferritic matrix.

In Fig. 10 the boundary maps corresponding to the same IPF maps presented in Fig. 10, for the different samples after SPCT, are shown. Red lines display misorientations between 10° and 49° and blue lines misorientations higher than 49° . Misorientations between 10° and 49° have been identified as grain boundaries developed during creep while misorientations higher to 49° belong to block boundaries of the martensitic microstructures. This description is supported by the fact that the boundaries between 10° and 49° delimit equiaxed grains and the boundaries higher than 49° define microstructures with an elongated or lath-like shape. In Fig. 10a it can be appreciated that, for the conventionally treated sample, the red boundaries, which are the boundaries

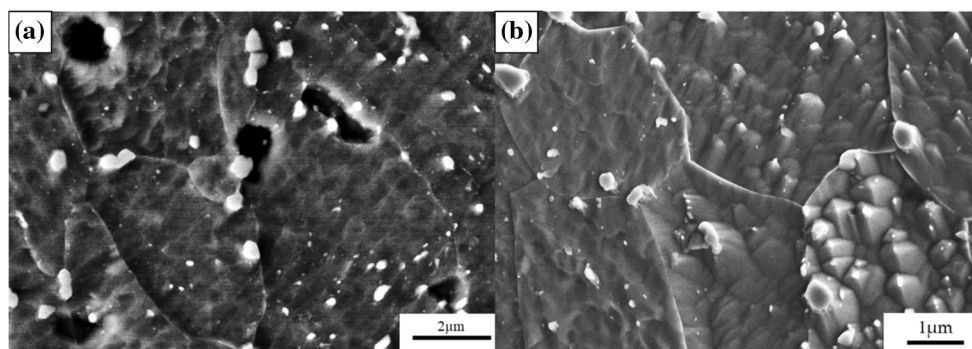


Fig. 7 Scanning electron microscopy images showing the presence of small grains formed during SPCT for the samples: **a** G91-TMT 900_20 and **b** G91-AR

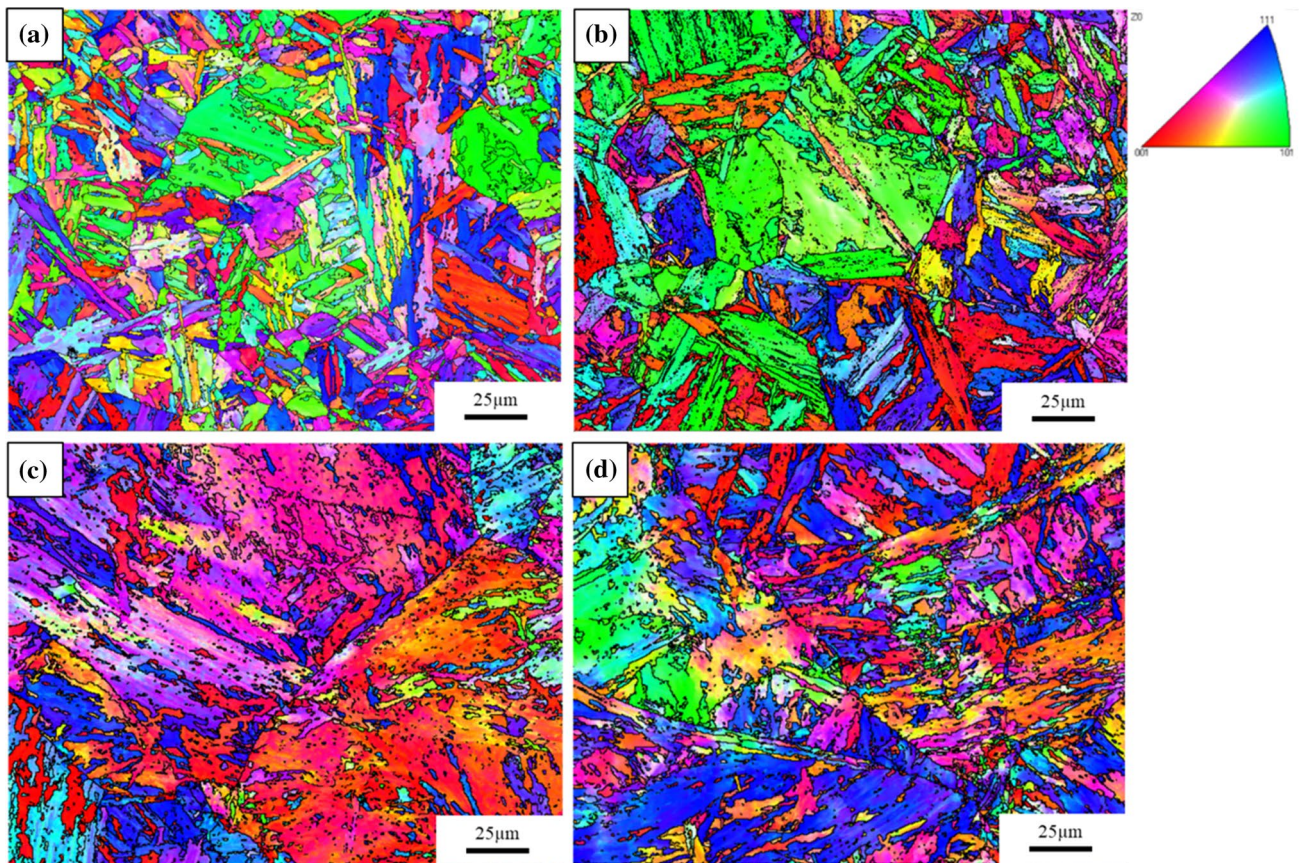


Fig. 8 Representative inverse pole figure (IPF) maps of the initial martensitic microstructure, for all the processing conditions investigated, prior to the SPCT: **a** G91-AR; **b** G91-TMT 900_20; **c** G91-TMT 600_20 and **d** G91-TMT 900_40

of the grains formed during creep, are distributed homogeneously. While, for the thermomechanically treated samples, these boundaries are heterogeneously distributed. As it has been discussed previously, these grains seem to be associated with the degradation process during creep as locations where the deformation accumulated have been larger. This fact is in agreement with the heterogeneous creep deformation suffered for the thermomechanically treated samples and the homogeneous creep deformation observed for the conventionally sample.

Figure 11 shows the grain boundary misorientation distributions for the conventionally treated sample and for the thermomechanically treated sample ausformed at 600 °C with a deformation of 20% before and after SPCT. Martensitic microstructures typically contain a high volume fraction of boundaries with their misorientation between 2.5° and 8° [26]. This is clearly distinguished for all the samples in both conditions, before and after SPCT. These misorientations have been reported to be related to lath boundaries and dislocations. It is important to mention that the step size used in the EBSD maps is too high to characterize the lath size or dislocation density properly, but it is enough to

observe the evolution of these microstructural features. Note that the frequency of these misorientations drops significantly after SPCT. Hence, during SPCT it may be suggested that recovery of dislocation and lath recovery/coarsening is taking place as suggested by Abe [7]. Besides, it is clearly observed that boundaries with the misorientations over the range 49°–62° have been reduced after SPCT. This result manifests that the blocks are coarsening during the SPCT. This behavior has been reported for the microstructural degradation during uniaxial creep tests [27, 28].

According to the results presented above, these creep microstructures have been developed by the progressive evolution of laths into new grains. Dislocations produced during creep are accumulated progressively in the laths low angle boundaries, leading to the increase of their misorientation angle and the formation of high angle boundaries (equiaxed grains). Taking into account the results shown previously in the SEM micrographs (Fig. 5a, b) the microstructural degradation would be a combined consequence of the accumulation of dislocation on the low angle boundaries and the stress concentration close to the coarse $M_{23}C_6$ carbides, which lead to the progressive loss of the lath-like

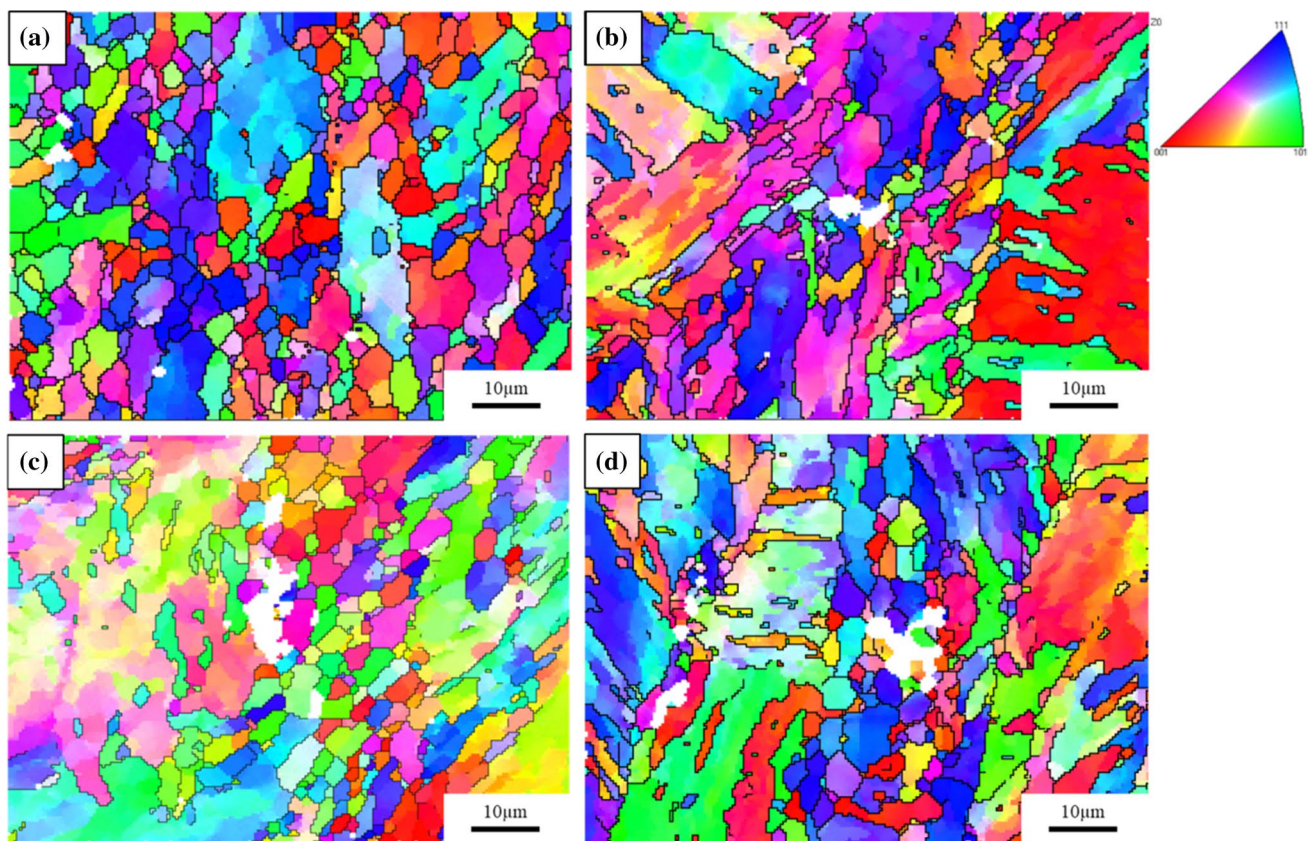


Fig. 9 Representative inverse pole figure (IPF) maps of the microstructures, for all the processing conditions investigated, after the SPCT: **a** G91-AR; **b** G91-TMT 900_20; **c** G91-TMT 600_20 and **d** G91-TMT 900_40

martensitic microstructure into equiaxed ferritic matrix. As it has been discussed above in the case of the thermomechanically treated samples, the nucleation of cavities takes place close to $M_{23}C_6$ precipitates located at the PAGB. The coalescence of the cavities would initiate the cracks and the final creep rupture through the prior austenite grain boundaries. The homogeneous coarsening of the $M_{23}C_6$ precipitates in the conventionally treated sample favors the apparition of equiaxed grains in all the martensitic matrix and develops the nucleation of cavities intragranularly which provokes the transgranular fracture.

Based on the results presented above and, taking into account the different stages of the thermomechanical treatments, the loss of creep ductility that enhances the change in fracture mechanism would be promoted mainly by the coarsening of $M_{23}C_6$ carbides at the vicinity of PAGB. The coarse $M_{23}C_6$ carbides located on prior austenite grain boundaries favor the nucleation of the cavities at the vicinity of the PAGB. Besides, in the TMT samples, the high austenitization temperature employed produces an enormous prior austenite grain size that remains large even after the thermomechanical treatments (much larger than the one obtained for the samples conventionally heat treated, Table 6). The

larger grain boundary surfaces present in the TMT samples compared to conventional ones facilitate an earlier reaching of the critical crack length, that causes the brittle fracture [29, 30].

Considering the improvement in creep strength achieved by the high number density of MX nanoprecipitates after thermomechanical treatment, in a future work the development of new alloys based on the optimization of the MX nanoprecipitates distribution will be explored bearing in mind that the prior austenite grain size has to be controlled during the processing route to avoid the loss in creep ductility which has been demonstrated to limit the use of these thermomechanical treatments.

4 Conclusions

The drop in creep ductility of G91 steel produced by changing the processing route from the conventional heat treatment to a thermomechanical treatment has been studied systematically and the main conclusions are summarized as follows:

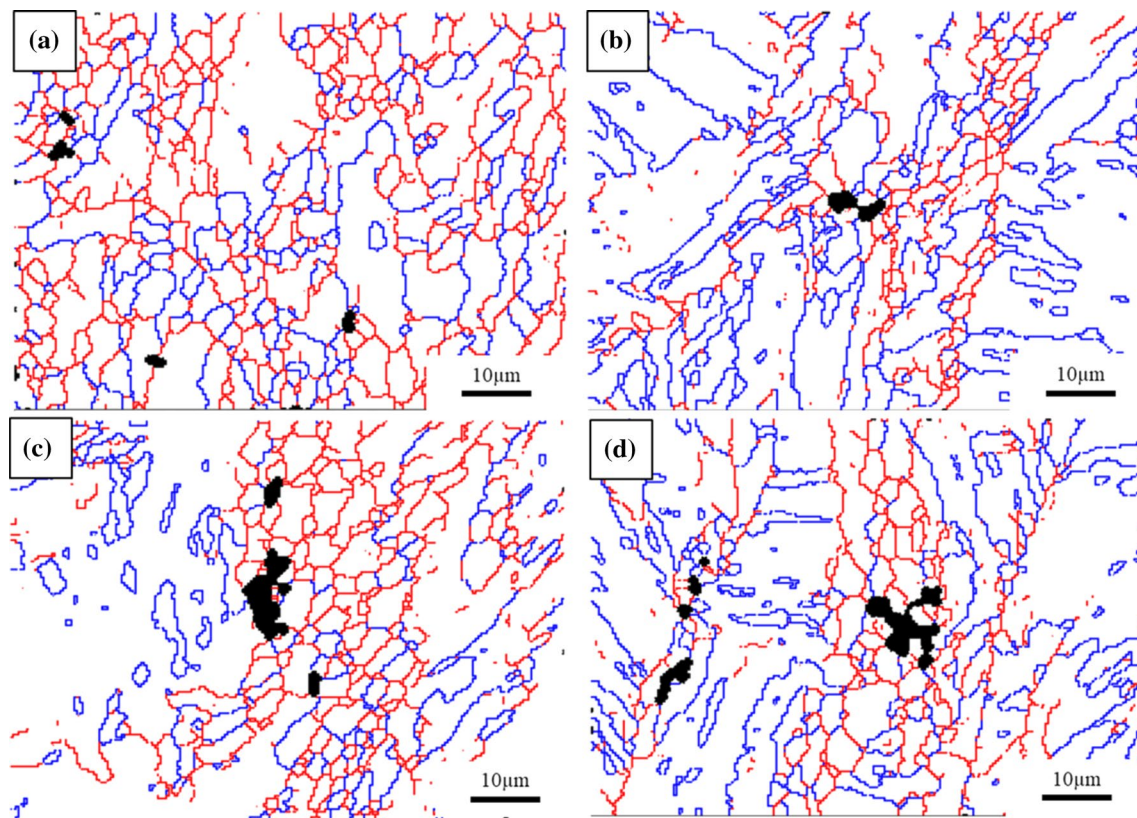


Fig. 10 Boundary maps, for all the samples investigated, after the SPCT: **a** G91-AR; **b** G91-TMT 900_20; **c** G91-TMT 600_20 and **d** G91-TMT 900_40. Red lines display misorientations between 10° and 49° and blue lines misorientations higher than 49°

1. The creep degradation leads, for both processing routes, to the full or partial substitution of the characteristic lath like morphology of martensitic microstructures by equiaxed grains. These grains are formed by the accumulation of dislocations on lath low angle boundaries, which produces an increase of their misorientation angle and the formation of high angle boundaries (between 10° and 49°), characteristic of these creep grains.
2. After the different thermomechanical treatments (TMT samples) most of the cavities are found close to coarse $M_{23}C_6$ carbides located at the vicinity of PAGB. This preferential coarsening of $M_{23}C_6$ carbides promote localized deformation in the vicinity of PAGB. The high resistance to dislocation movement inside the grains produced by the high number density of MX nanoprecipates could also contribute to promote localized deformation. By contrast, after the conventional heat treatment the cavities appeared homogeneously distributed in the sample which implies an homogeneous creep deformation.
3. The preferential microstructural degradation at the vicinity of the PAGB for the thermomechanically treated samples produced fracture surfaces without dimples and the presence of some cleavage surfaces, suggesting an intergranular brittle fracture. While, the sample after the conventional heat treatment showed a homogeneous microstructural degradation and a transgranular ductile fracture with the presence of dimples.
4. After the nucleation and coalescence of the cavities the propagation of the cracks was facilitated by the much larger prior austenite grain size of the thermomechanically treated samples compared to the conventional ones, which favors the propagation of the cracks along grain boundaries triggering the intergranular brittle fracture. The different propagation paths of the cracks in these samples produces a change in the fracture mechanism from transgranular ductile fracture for the conventionally treated sample to brittle intergranular fracture for the thermomechanical treated ones, leading to a reduction in the creep ductility that limits the potential use of the proposed thermomechanical processing routes.

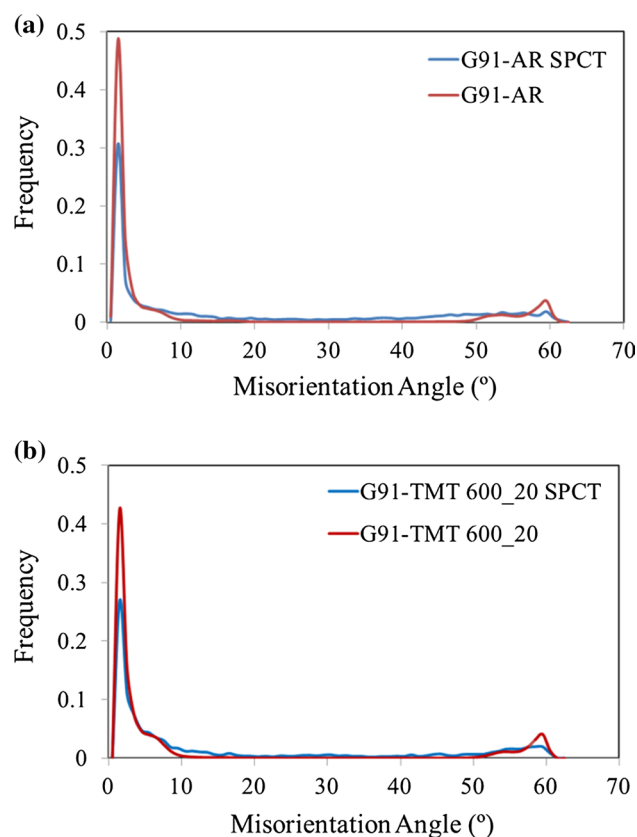


Fig. 11 Grain boundary misorientation distributions for samples: **a** G91-AR and **b** G91-TMT 600_20. The results before (red) and after (blue) the SPCT are provided for comparison

Table 6 Prior austenite grain size for the conventionally and thermo-mechanically treated samples

Samples	Prior austenite grain size (μm)
G91-AR	43 ± 4
G91-TMT 900_20	141 ± 19
G91-TMT 900_40	128 ± 17
G91-TMT 600_20	259 ± 13

5 Data Availability

The raw/processed data required to reproduce these findings cannot be shared at this time as the data also forms part of an ongoing study.

Acknowledgements Authors acknowledge financial support to Ministerio de Economía y Competitividad (MINECO) through in the form of a Coordinate Project (MAT2016-80875-C3-1-R). Authors also would like to acknowledge financial support to Comunidad de Madrid through DIMMAT-CM_S2013/MIT-2775 project. The authors are grateful for the dilatometer tests by Phase Transformation laboratory. J.Vivas acknowledges financial support in the form of a FPI Grant BES-2014-069863. This work contributes to the Joint Programme on Nuclear Materials (JPNM) of the European Energy Research Alliance (EERA).

References

1. R.L. Klueh, D.S. Gelles, S. Jitsukawa, A. Kimura, G.R. Odette, B. van der Schaaf, M. Victoria, J. Nucl. Mater. **307–311**(Part 1), 455–465 (2002)
2. R.L. Klueh, K. Ehrlich, F. Abe, J. Nucl. Mater. **191–194**(Part A), 116–124 (1992)
3. L. Tan, Y. Katoh, A.A.F. Tavassoli, J. Henry, M. Rieth, H. Sakasegawa, H. Tanigawa, Q. Huang, J. Nucl. Mater. **479**, 515–523 (2016)
4. F. Masuyama, ISIJ Int. **41**, 612–625 (2001)
5. S.J. Zinkle, G.S. Was, Acta Mater. **61**, 735–758 (2013)
6. F. Abe, T. Horiuchi, M. Taneike, K. Sawada, Mater. Sci. Eng. A **378**, 299–303 (2004)
7. F. Abe, Mater. Sci. Eng. A **387**, 565–569 (2004)
8. F. Abe, Engineering **1**, 211–224 (2015)
9. S. Hollner, B. Fournier, J. Le Pendu, T. Cozzika, I. Tournié, J.C. Brachet, A. Pineau, J. Nucl. Mater. **405**, 101–108 (2010)
10. M. Song, C. Sun, Z. Fan, Y. Chen, R. Zhu, K.Y. Yu, K.T. Hartwig, H. Wang, X. Zhang, Acta Mater. **112**, 361–377 (2016)
11. J. Vivas, C. Celada-Casero, D. San Martín, M. Serrano, E. Urones-Garrote, P. Adeva, M.M. Aranda, C. Capdevila, Metall. Mater. Trans. A **47**, 1–8 (2016)
12. M. Tamura, H. Sakasegawa, A. Kohyama, H. Esaka, K. Shinozuka, J. Nucl. Mater. **321**, 288–293 (2003)
13. J. Vivas, C. Capdevila, E. Altstadt, M. Houska, M. Serrano, D. De-Castro, D. San-Martín, Mater. Sci. Eng. A **728**, 259–265 (2018)
14. S. Holdsworth, Mater. High Temp. **34**, 97–98 (2017)
15. J. Parker, Mater. High Temp. **34**, 109–120 (2017)
16. E.N. Campitelli, P. Spätig, R. Bonadé, W. Hoffelner, M. Victoria, J. Nucl. Mater. **335**, 366–378 (2004)
17. Y. Ruan, P. Spätig, M. Victoria, J. Nucl. Mater. **307**, 236–239 (2002)
18. D.J. Brookfield, W. Li, B. Rodgers, J.E. Mottershead, T.K. Hellen, J. Jarvis, R. Lohr, R. Howard-Hildige, A. Carlton, M. Whelan, J. Strain Anal. Eng. Des. **34**, 423–436 (1999)
19. M.P. Manahan, A.S. Argon, O.K. Harling, J. Nucl. Mater. **104**, 1545–1550 (1981)
20. E. Altstadt, M. Serrano, M. Houska, A. García-Junceda, Mater. Sci. Eng. A **654**, 309–316 (2016)
21. E. Altstadt, H.E. Ge, V. Kuksenko, M. Serrano, M. Houska, M. Lasan, M. Bruchhausen, J.M. Lapetite, Y. Dai, J. Nucl. Mater. **472**, 186–195 (2016)
22. J. Vivas, C. Capdevila, E. Altstadt, M. Houska, D. San-Martín, Scr. Mater. **153**, 14–18 (2018)
23. T. De Cock, C. Capdevila, F.G. Caballero, C. García de Andrés, Mater. Sci. Eng. A **519**, 9–18 (2009)
24. Y. Sugino, S. Ukai, B. Leng, N. Oono, S. Hayashi, T. Kaito, S. Ohtsuka, Mater. Trans. **53**, 1753–1757 (2012)
25. J. Vivas, C. Capdevila, J. Jimenez, M. Benito-Alfonso, D. San-Martín, Metals **7**, 236 (2017)
26. P.P. Suikkanen, C. Cayron, A.J. DeArdo, L.P. Karjalainen, J. Mater. Sci. Technol. **27**, 920–930 (2011)
27. A. Fedoseeva, N. Dudova, R. Kaibyshev, J. Mater. Sci. **52**, 2974–2988 (2017)
28. D. Rojas, J. Garcia, O. Prat, L. Agudo, C. Carrasco, G. Sauthoff, A.R. Kaysser-Pyzalla, Mater. Sci. Eng. A **528**, 1372–1381 (2011)
29. T.L. Anderson, *Fracture Mechanics: Fundamentals and Applications* (Taylor & Francis/CRC Press, Boca Raton, 2005)
30. E. Plesiutchnig, C. Beal, S. Paul, G. Zeiler, C. Sommitsch, Mater. High Temp. **32**, 318–322 (2015)